

Upper-Ocean Heat and Salt Balances in the Western Equatorial Pacific in Response to the Intraseasonal Oscillation during TOGA COARE*

MING FENG,⁺ ROGER LUKAS, AND PETER HACKER

School of Ocean and Earth Science and Technology, University of Hawaii, Honolulu, Hawaii

ROBERT A. WELLER AND STEVEN P. ANDERSON

Woods Hole Oceanographic Institution, Woods Hole, Massachusetts

(Manuscript received 12 April 1999, in final form 30 August 1999)

ABSTRACT

During the TOGA COARE Intensive Observing Period (IOP) from November 1992 through February 1993, temperature, salinity, and velocity profiles were repeatedly obtained within a 130 km × 130 km region near the center of the Intensive Flux Array (IFA) in the western equatorial Pacific warm pool. Together with high quality measurements of air–sea heat flux, rain rate, upper-ocean microstructure, and penetrating solar radiation, they make up a unique dataset for upper-ocean heat and freshwater budget studies. Three survey cruises sampled different phases of the Intraseasonal Oscillation (ISO) during the IOP. Temporal evolution and advective terms in the heat and salt balance equations, on timescales of 3 days and longer, are estimated using the survey data. The upper-ocean (0–50 m) heat and salt budgets at the center of the IFA were estimated and are closed to within 10 W m⁻² of observed air–sea heat fluxes and to within approximately 20% of observed rain rates during each of the three cruises. Generally, advection in the upper ocean cannot be neglected during the IOP. Zonal advection alternates sign but had a net warming and freshening tendency. Meridional advection decreased temperature and increased salinity in the surface layer, while vertical advection warmed and freshened the surface layer because of the general downwelling trend. Heat advection is as important as the net air–sea flux during the westerly wind burst time periods. The sub-ISO timescale upper-ocean dynamics, such as the strong meridional advection caused by inertial motions, are found to have important contributions to the upper-ocean heat and freshwater balances.

1. Introduction

The Tropical Ocean Global Atmosphere (TOGA) program conducted its Coupled Ocean–Atmosphere Response Experiment (COARE) in the Intensive Flux Array (IFA, Fig. 1) during the Intensive Observing Period (IOP) from November 1992 through February 1993 (Webster and Lukas 1992). It provided a unique dataset to study the Intraseasonal Oscillation (ISO) variability and its impacts on the evolution of the coupled ocean–atmosphere system in the western equatorial Pacific warm pool. With the ongoing El Niño–Southern Oscil-

lation event, strong ISO variability was observed during the IOP (Lukas et al. 1995; Weller and Anderson 1996; Godfrey et al. 1998).

The warm pool region is unique in that surface heat and freshwater fluxes contribute equally to the net surface buoyancy flux into the ocean. The net freshwater flux of about 1.5 m yr⁻¹ (Donguy 1987) forms a salt-stratified barrier layer in the often nearly isothermal upper ocean and makes the warm pool sea surface temperature (SST) more sensitive to local air–sea interactions (Lukas and Lindstrom 1991; Sprintall and Tomczak 1992). In addition, much of the air–sea flux variability is modulated on intraseasonal timescales (Webster and Lukas 1992). Prior to TOGA COARE, attempts to close the long-term mean surface energy budget in the warm pool were of limited success and were left with errors of 60–80 W m⁻² (Godfrey and Lindstrom 1989). These early studies used available merchant ship data, which did not resolve the energetic intraseasonal variability in the region. In addition, they lacked accurate air–sea flux measurements and parameterizations. The combined surface and ocean datasets from ships and buoys during TOGA COARE provide for the first time the ability to accurately study

* School of Ocean and Earth Science and Technology Contribution No. 5206 and Woods Hole Oceanographic Institution Contribution No. 10036.

⁺ Current affiliation: CSIRO Division of Marine Research, Hobart, Tasmania, Australia.

Corresponding author address: Dr. Ming Feng, CSIRO Division of Marine Research, GPO Box 1538, Castray Esplanade, Hobart, Tasmania 7001, Australia.
E-mail: ming.feng@marine.csiro.au

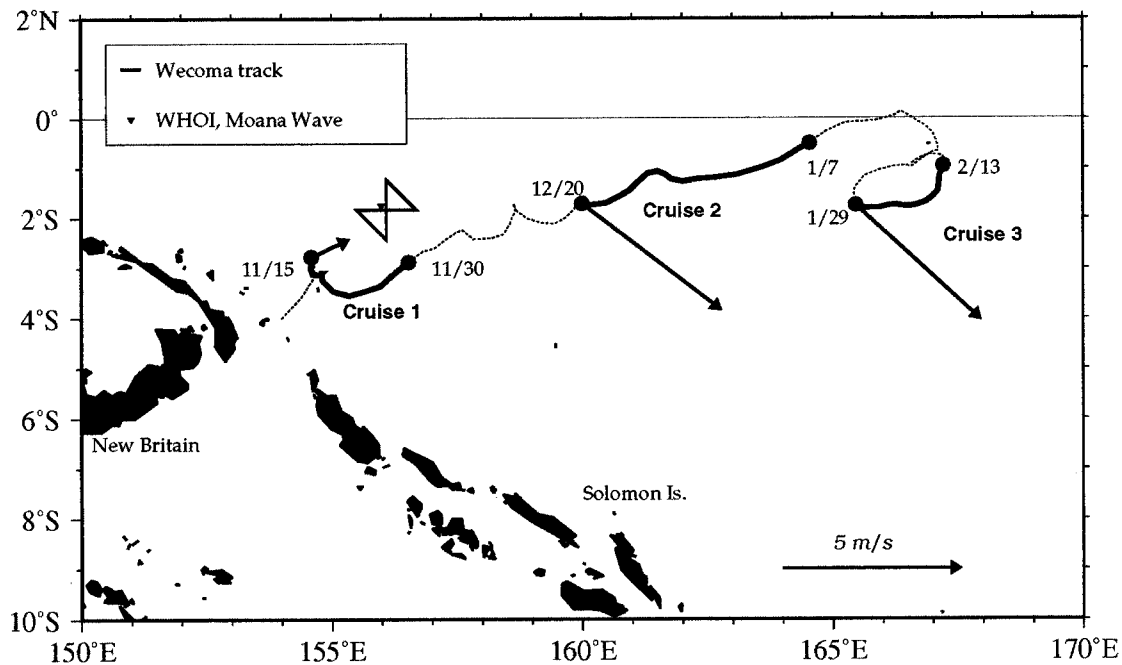


FIG. 1. Map of study region and R/V *Wecoma* survey pattern. The curve is the progressive plot of the 5-m currents observed at the WHOI mooring during the IOP (solid segments indicate the time periods of the budget calculations). The arrows indicate the cruise-mean winds. The inverted triangle indicates the position of the WHOI mooring and the R/V *Moana Wave*.

the warm pool energy budgets, especially in response to the ISO forcing.

COARE air–sea flux measurements have determined the net heat flux in the IFA with an accuracy better than 10 W m^{-2} averaged over a few weeks (Fairall et al. 1996; Weller and Anderson 1996; Bradley and Weller 1997). However, the IOP mean rain-rate estimates from different methods vary from 4.5 to 11.3 mm day^{-1} (Godfrey et al. 1998), though some of the discrepancy is due to different time and space coverage (Johnson and Ciesielski 2000). Comparison of coincident, collocated rain data indicates that different rain measurements agreed within 20% (Bradley and Weller 1997). The high quality air–sea heat flux observations provide an opportunity to test the heat budget calculation from the ocean data, while the freshwater budget closure during the IOP provides an independent estimate of the rain rate to compare with estimates from in situ rain gauges, shipboard radars, satellite algorithms, and atmospheric moisture budgets.

Although 1D processes could account for the upper-ocean heat balance during most of the IOP, there were significant deviations especially during westerly wind burst (WWB) periods (Anderson et al. 1996; Ralph et al. 1997). In order to explain the upper-ocean freshwater (salt) balance, 1D processes were generally not adequate (Anderson et al. 1996; Cronin and McPhaden 1998). Zonal advection was identified to be important to the long-term heat and freshwater balances near the equator (Ralph et al. 1997; Cronin and McPhaden 1997, 1998). Feng et al. (1998a; hereafter called FHL98) concluded that the meridional advection due to inertial motions

had significant impacts on the upper-ocean heat and salt balances at 2°S during the December 1992 WWB. By using the improved air–sea flux data and considering the advective terms, the upper-ocean heat budget was balanced within 10 W m^{-2} and the upper-ocean salt budget agreed well with in situ rain-rate measurement (FHL98). Richards and Inall (2000) also found the importance of meridional advection during the same time period from a different dataset. However, calculations from SST gradients seem to have underestimated this meridional heat advection (Ralph et al. 1997).

The present study, which extends the analysis in FHL98 to the whole IOP survey period, uses data collected in the center of the IFA to examine the meridional advection as well as the other advective terms in response to the ISO. This paper is organized as follows. In section 2, we describe the data and the method used in this study; in section 3, we present the advection and budget calculation results; and in section 4, the results are discussed and our conclusions are stated.

2. Data and analysis methods

During the IOP, the R/V *Wecoma* surveyed the upper ocean in the IFA repeatedly along a butterfly pattern centered at 1.8°S , 156.1°E (Fig. 1), with a spatial extent of 130 km in both zonal and meridional directions and a repeat time of 1.5 days. Nearly continuous acoustic Doppler current profiler (ADCP) and Seasoar/CTD temperature and salinity measurements were made along the ship track. The *Wecoma* observations within the IFA

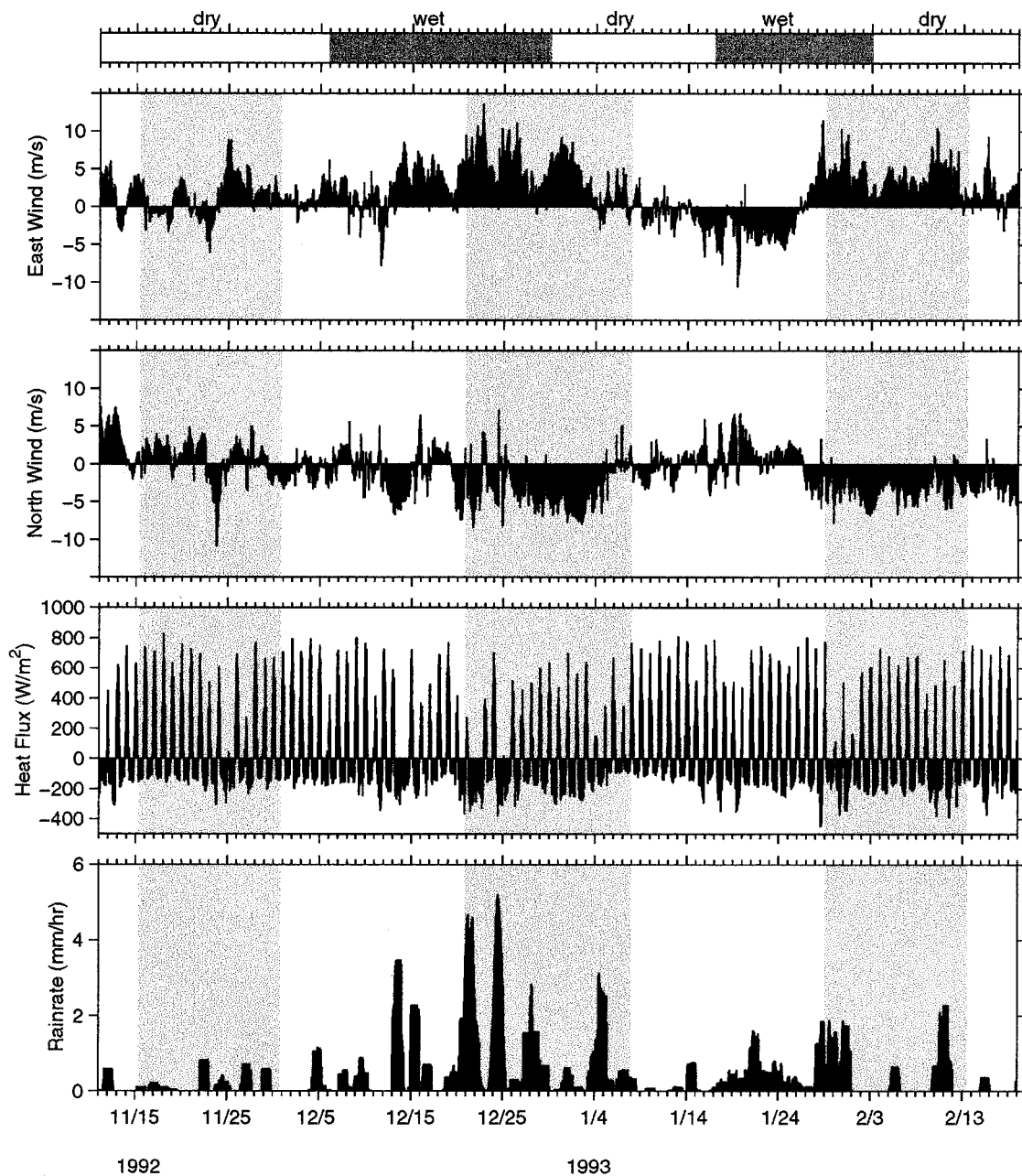


FIG. 2. The eastward and northward wind speeds, the net surface heat flux, and the rain rate during the IOP from the WHOI mooring data. The shaded areas indicate the budget calculation time periods for the three cruises of the repeated surveys. On the top panel, we indicate the “dry” and “wet” phases of the ISO (Lau and Sui 1997).

were collected during three cruises (Huyer et al. 1997). In the present study, budget calculations are carried out for three time periods: 15–30 November 1992 (cruise 1), 20 December 1992–7 January 1993 (cruise 2), and 29 January–13 February 1993 (cruise 3) (Fig. 2). Detailed information about the *Wecoma* data are in Huyer et al. (1997) and FHL98.

Air–sea flux observations were made aboard the *Wecoma*, at a central surface mooring (deployed by Woods Hole Oceanographic Institution, hereafter called the

WHOI mooring) and aboard the R/V *Moana Wave* during the IOP. The WHOI mooring was located at $1^{\circ}45'S$, $156^{\circ}E$, and the *Moana Wave* was stationed within 10 km of the WHOI mooring, both near the center of the *Wecoma* butterfly survey pattern (Fig. 1). Using the Fairall et al. (1996) COARE 2.5b bulk flux algorithm, the air–sea heat flux was estimated from the WHOI mooring and *Wecoma* measurements (Weller and Anderson 1996; C. Paulson 1998, personal communication; Bradley and Weller 1997). A recent precision infrared

radiometer evaluation by Fairall et al. (1998) led to an increase of the reference longwave radiation data by 7 W m^{-2} . For the present study, therefore, the WHOI net surface heat flux has been increased by 7 W m^{-2} over the values originally given by Weller and Anderson (1996). The same correction was applied in FHL98. Rain rates were measured by the *Wecoma* syphon rain gauge and optical rain gauge (ORG; C. Paulson 1998, personal communication), and by the *Moana Wave* ORG (Fairall et al. 1996). The sensible heat flux due to rainfall was calculated from the *Moana Wave* and the *Wecoma* measurements (Fairall et al. 1996) to correct the net heat

flux. To evaluate the vertical turbulent fluxes in the upper ocean, microstructure measurements were made with the advanced microstructure profiler (AMP) from 11 November to 3 December 1992 during cruise 1 (Wijesekera and Gregg 1996) and with the CHAMELEON profiler from 20 December 1992 to 12 January 1993 during cruise 2 (Smyth et al. 1996) on the *Moana Wave*. During cruise 3, a few deep AMP casts were made from 28 January to 5 February 1993 (Gregg et al. 1994), which are not used in the present study.

Following FHL98, the heat and salt tendency equations, vertically integrated from the sea surface to a fixed water depth, are written as

$$\begin{aligned} \overbrace{Q_0 - R_s|_{-h}}^{\text{surface forcing}} &= \overbrace{\int_{-h}^0 \rho_0 c_p \frac{\partial T}{\partial t} dz - F_T|_{-h}}^{\text{1D processes}} + \overbrace{\int_{-h}^0 \rho_0 c_p \left(u \frac{\partial T}{\partial x} + v \frac{\partial T}{\partial y} + w \frac{\partial T}{\partial z} \right) dz}^{\text{advective terms}} \quad (1a) \\ -(P - E) &= \frac{1}{S_0} \overbrace{\int_{-h}^0 \frac{\partial S}{\partial t} dz - \frac{F_s|_{-h}}{S_0}}^{\text{1D processes}} + \frac{1}{S_0} \overbrace{\int_{-h}^0 \left(u \frac{\partial S}{\partial x} + v \frac{\partial S}{\partial y} + w \frac{\partial S}{\partial z} \right) dz}^{\text{advective terms}}, \quad (1b) \end{aligned}$$

where $z = 0$ is the sea surface; h is the depth of the lower boundary (here selected to be 50 m); T and S are temperature and salinity; ρ_0 is the mean water density; c_p is the specific heat capacity of seawater at constant pressure; u , v , and w are the zonal, meridional, and vertical velocities; and positive x , y , and z are eastward, northward, and upward, respectively. Here $Q_0 = R_s(0) + F_T(0)$ is the net surface heat flux, where $R_s(0)$ is the net surface shortwave (solar) radiation flux and $F_T(0)$ includes net longwave radiation flux, latent heat flux, sensible heat flux, and the heat flux due to rainfall. Positive Q_0 corresponds to ocean heating. Here $R_s|_{-h}$ is the penetrating solar radiation at depth h , which for this analysis is set at 50 m. The transmission through 50 m is set to a constant value of 4.3% (Anderson et al. 1996), although it actually varies with time (Siegel et al. 1995). The variation may affect the 0–20-m heat budget considerably, but the effect is much smaller for the 0–50-m average. Here S_0 is the surface salinity, and P and E are the precipitation and evaporation rates. Here $F_T|_{-h} = -\rho c_p K_T \partial T / \partial z$ and $F_s|_{-h} = -K_S \partial S / \partial z$ are the vertical turbulent heat and salt fluxes at depth h . The thermal and haline diffusivities are set equal to the density diffusivity, $K_T = K_S = K_\rho = \Gamma \epsilon / N^2$, where $\epsilon(z, t)$ is the turbulent kinetic energy dissipation rate calculated from the microstructure measurements (Smyth et al. 1996). Here $N(z, t) = [-g \partial \rho(z, t) / \rho_0 \partial z]^{1/2}$ is the buoyancy frequency and $\Gamma = 0.2$ is the mixing efficiency (Moum 1990). The mixing efficiency selection is confirmed by large-eddy simulation results (Skylingstad et al. 1999).

Because turbulent flux-related observations are not

available during cruise 3 for the IFA, a Richardson number-based turbulent parameterization, tested against microstructure measurements (Soloviev et al. 2000, manuscript submitted to *J. Geophys. Res.*) is used to estimate the vertical turbulent heat and salt diffusivities at 50 m. Thus $K_T = K_S = \kappa u_* z (1 - \alpha \text{Ri})^{1/4} \theta(-\text{Ri}) + \kappa u_* z (1 - \text{Ri} / \text{Ri}_{\text{cr}}) \theta(1 - \text{Ri} / \text{Ri}_{\text{cr}}) \theta(\text{Ri}) + K_{\text{mt}}$, where $\kappa = 0.4$, u_* is friction velocity of the wind forcing, z is water depth, Ri is the gradient Richardson number, $\alpha = 15$, $\theta(x) = 1$ at $x > 0$ and $\theta(x) = 0$ at $x \leq 0$, $\text{Ri}_{\text{cr}} = 0.25$ is the critical Richardson number, and K_{mt} (in units of $\text{m}^2 \text{s}^{-1}$) = $5 \times 10^{-4} (1 + 5 \text{Ri})^{-1.5} + 2 \times 10^{-5}$. For the calculation 4-hour averaged *Wecoma* data are used.

The selection of 50 m as the lower boundary is consistent with the nighttime mixed layer depth and minimizes the influence of thermocline displacements on the budget calculation (FHL98). Coincidentally, based on drifter data, Ralph et al. (1997) found that 50 m was the effective scale depth of the surface heat and momentum fluxes. In FHL98, it was also shown that the budget calculations were not sensitive to the selection of the lower boundary within the range of 40–60 m for cruise 2.

The advective terms are calculated from a linear fit of the *Wecoma* data over every two complete butterfly circuits (approximately 3 days) (FHL98). That is, we evaluate $d[x(t), y(t), t] = \bar{d} + d_x x + d_y y + d_t t + d'[x(t), y(t), t]$, where $d = d[x(t), y(t), t]$ is the variable to be fit; x and y are the longitude and latitude relative to the crossover point, respectively; t is the time relative to the center time of the interval; \bar{d} , d_x , d_y , and d_t are

TABLE 1. The 0–50-m heat budget closure.

	Cruise 1 15–30 Nov 1992	Cruise 2 20 Dec 1992– 7 Jan 1993	Cruise 3 29 Jan– 13 Feb 1993
Temporal change	53	–88	–9
GTotal advection	1	43	–18
Zonal	–9	–13	3
Meridional	18	65	8
Vertical	–8	–9	–29
Turbulent flux	0	11	12
Estimated $Q_0 - R_s(-h)$	54	–34	–15
$R_s(-h)$ <i>Wecoma</i> (WHOI)	9(9)	7(7)	9(8)
Estimated Q_0	63(63)	–27(–27)	–6(–7)
Q_0 <i>Wecoma</i> (WHOI)	66(68)	–28(–28)	–12(–11)
Residual	–3(–5)	1(1)	6(4)

Units: $W m^{-2}$.

constants; and d' is the residual. In this sense, the \bar{d} represents the mean value of d at the crossover point; d_x and d_y represent the mean zonal and meridional gradients, respectively; and d_t is the mean rate of temporal change over the interval. The vertical velocity is calculated from the weighted combination of the velocity divergence method $w = -\int_{z_0}^z (\partial u/\partial x + \partial v/\partial y) dz$ and the density method $w(\partial \rho/\partial z) = -\partial \rho/\partial t - u(\partial \rho/\partial x) - v(\partial \rho/\partial y)$ (FHL98), where the weighting is inversely proportional to the standard error of each estimate.

In the heat equation, the surface forcing term includes the net surface heat flux and the penetrating solar radiation at 50 m. The surface forcing in the salt equation is the difference between precipitation and evaporation rates. The balance between the surface forcing and the 1D processes (the temporal changes of temperature and salinity averaged over the upper 50 m and the vertical turbulent fluxes of heat and salt at 50 m) are termed the “1D budget.” By evaluating the 1D process terms (1D budget) or the 1D processes plus advective terms (3D budget) on the right-hand side of Eqs. 1, the surface forcing terms on the left-hand sides are estimated independently of the air–sea flux estimates.

3. Results

a. Air–sea fluxes

The IOP as used in this paper refers to the 100 days from 11 November 1992 to 18 February 1993, covering the three survey cruises of the R/V *Wecoma* (Fig. 2). During the IOP, there are two active phases of the ISO events characterized by deep convection and heavy rainfall, described as the wet phase of the ISO by Lau and Sui (1997). The ISOs are also related to strong WWBs (Weller and Anderson 1996). The two WWB events during the two active ISOs occur in late December 1992 and in late January–February 1993. There is an easterly wind period before the late January–February WWB. The upper ocean receives heat at the air–sea interface during the suppressed phase of the ISO; during the active phase it loses heat to the atmosphere due to cloud

TABLE 2. The 0–50-m freshwater budget closure.

	Cruise 1 15–30 Nov 1992	Cruise 2 20 Dec 1992– 7 Jan 1993	Cruise 3 29 Jan– 13 Feb 1993
Temporal change	–5.8	7.3	1.6
Total advection	7.5	–11.5	5.0
Zonal	7.2	–1.2	–1.1
Meridional	–0.3	–14.8	–2.9
Vertical	0.6	4.5	9.0
Turbulent flux	–0.9	–6.5	–6.9
Estimated $P - E$	–0.8	10.7	0.3
E <i>Wecoma</i> (WHOI)	3.0(3.0)	4.5(4.3)	4.8(4.7)
Estimated P	2.2(2.2)	15.2(15.0)	5.1(5.0)
P (<i>Wecoma</i> syphon)	1.8	12.8	2.9
P (<i>Wecoma</i> ORG)	3.0	16.4	6.5
P (<i>Moana Wave</i> ORG)	3.8	17.8	Out of IFA

Units: $mm day^{-1}$.

blocking of the solar radiation and enhanced evaporative cooling while gaining freshwater through heavy rainfall (Weller and Anderson 1996; Godfrey et al. 1998). The sensible heat flux, and the variation in net longwave radiation, are significant, though smaller on average, than other terms.

Cruise 1 was during the suppressed phase of the ISO, with relatively calm wind, though there was a short episode of westerly wind on 25 November (Fig. 2). Cruise 2 captured the strong multipeak December WWB and the following low wind period. Throughout cruise 3, the frequent and short-lived moderate southeastward wind bursts or squalls (Weller and Anderson 1996) dominated. The mean wind speeds are 3.1, 5.3, and 5.0 $m s^{-1}$, for the three cruises, respectively. The vector mean wind speeds are 1.2, 4.9, and 4.8 $m s^{-1}$, and the mean wind directions are toward 64°, 127°, and 133°, respectively, for the three cruises (Fig. 1).

At the air–sea interface, the net ocean heat gain is 66 $W m^{-2}$ during cruise 1 (Table 1). The surface heat losses during cruises 2 and 3 are –28 and –12 $W m^{-2}$, respectively. The cruise mean net heat fluxes computed from the WHOI data differ at most by 2 $W m^{-2}$ from those computed for the *Wecoma* data. Cruise 3 is much less cloudy than cruise 2 so that there is greater heat gain from solar forcing. The cruise mean rain rates are 1.8, 12.8, and 2.9 $mm day^{-1}$ from the *Wecoma* syphon gauge, and 3.0, 16.4, and 6.5 $mm day^{-1}$ from the *Wecoma* ORG (Table 2). The *Moana Wave* ORG measured slightly higher rain rates than the *Wecoma* ORG during cruises 1 and 2, and the *Moana Wave* was outside of the IFA during most of cruise 3. Note the systematic differences between the ORG and syphon gauge measurements (Bradley and Weller 1997).

The three time periods for budget calculations cover approximately half of the total IOP. The *Wecoma* surveys are biased toward the westerly wind periods (Fig. 3); relatively more westerlies occur during the *Wecoma* surveys than during the IOP as measured at the WHOI buoy. Also the *Wecoma* did not sample the easterly wind

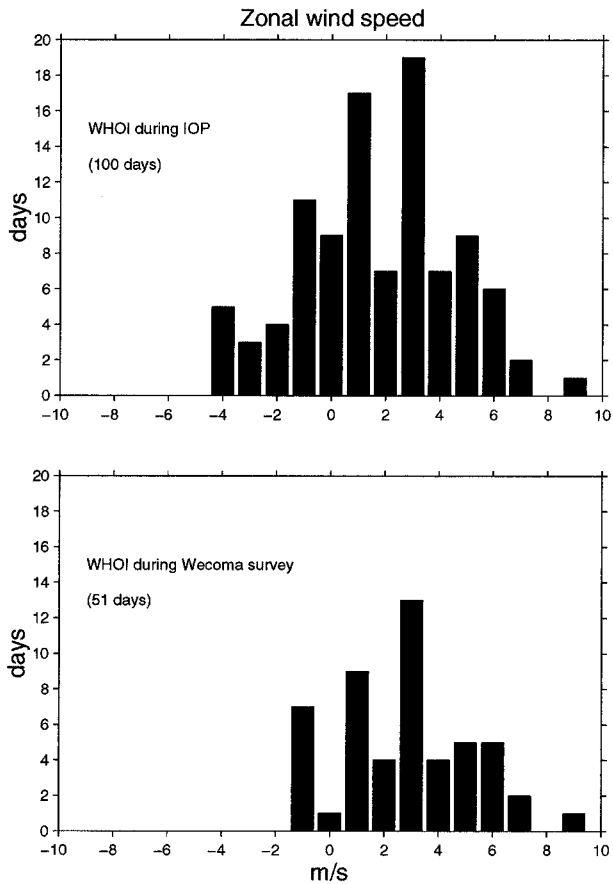


FIG. 3. The frequency distributions of the zonal wind speed from the WHOI data during the IOP and during the repeated surveys.

in the middle of January 1993 between the two WWBs (Fig. 2).

b. Upper-ocean variability

The IOP mean (11 November 1992 to 18 February 1993) zonal and meridional current velocities at 5 m are 0.16 m s^{-1} and 0.04 m s^{-1} , respectively, implying advective distances of 1395 and 341 km to the east and north (Fig. 1). Thus, the ratio between the zonal and meridional scales of advection is 4:1 near the sea surface. The ratio decreases almost linearly to one at 50 m from the WHOI mooring subsurface data (Pludde-mann et al. 1993). The mean current direction at the sea surface is 47° to the left of the mean wind direction during the IOP. There are variable near-inertial motions superimposed upon this east-northeastward trajectory (Fig. 1). The 10–15-day period meridional excursions were also identified from surface drifter trajectories (Ralph et al. 1997). Coherent vertical propagation of near-inertial energy is detected in other COARE mooring data (Eriksen et al. 1998).

There is one eastward surface pulse during cruise 1,

two pulses during cruise 2, and one pulse during cruise 3 in response to the westerlies (Fig. 4), mostly confined in the upper 50 m. This is consistent with the scale depth derived from the drifter data (Ralph et al. 1997). The Coriolis force turns the current northward in the aftermath of the WWBs. The strongest eastward jet during the IOP ($>0.5 \text{ m s}^{-1}$) occurs in response to the last peak of the December 1992 WWB. The northward inertial flow related to this jet is also the strongest, with a sub-surface core of more than 0.3 m s^{-1} near 50 m (Fig. 4). It is notable that the eastward surface jet is much weaker during cruise 3 than cruise 2, although the wind speeds during the two cruises are similar (Fig. 1). There are several reasons for this: The mass accumulation due to the previous eastward jets set up a pressure gradient to counter the wind stress; the surface mixed layer is deepened so that the momentum is distributed over a larger vertical depth; and the current is initially westward in cruise 3 while eastward in cruise 2 so that their initial conditions are different. This is in contrast to cruise 1 when a stronger surface jet is generated by relatively weaker westerly wind, owing to the strong near-surface stratification trapping the momentum flux. The detailed momentum budget requires further analysis. The sub-surface reversing jet below 70 m (Zhang and Rothstein 1998) also tends to accelerate during the WWBs of cruises 1 and 2, with a peak speed above 0.2 m s^{-1} (Fig. 4), which may be due to high mode equatorial waves (Richardson et al. 1999).

The vertical velocity generally alternates between upwelling and downwelling episodes (Fig. 4), reflecting vertical motions related to low-frequency internal waves. Instantaneous vertical velocity has a magnitude of 10 m day^{-1} . Downwelling is more prominent in the upper 100 m during the three cruises (Fig. 5). The mean vertical velocity during cruise 1 is less than 1 m day^{-1} over the upper 100 m, with net downwelling in the upper 50 m. During cruise 2, the mean vertical velocity has a peak downwelling at 50 m greater than 2 m day^{-1} , then reduces to near zero at 100 m. The mean downwelling during cruise 3 steadily increases downward from the surface to more than 1 m day^{-1} at 100 m. This is mostly due to the downwelling episode at the beginning of the cruise (Fig. 4), which is also observed over a larger meridional scale (Eldin et al. 1994). The vertical velocity in the surface layer near the equator largely depends on the zonal wind direction according to the Yoshida jet solution (Gill 1982). The biased sampling of zonal wind shown earlier (Fig. 3) may explain the mean downwelling in the surface layer for all three survey cruises.

The top of the thermocline is near 60–80 m in the IFA (Fig. 6). The 28°C isotherm, whose mean depth coincides with the 34.6 psu isohaline, can be used to represent the top of the pycnocline (Fig. 7). In the pycnocline above 100 m, the temperature decreases monotonically with depth, while the salinity increases monotonically with depth; both trends intensify the pycnoc-

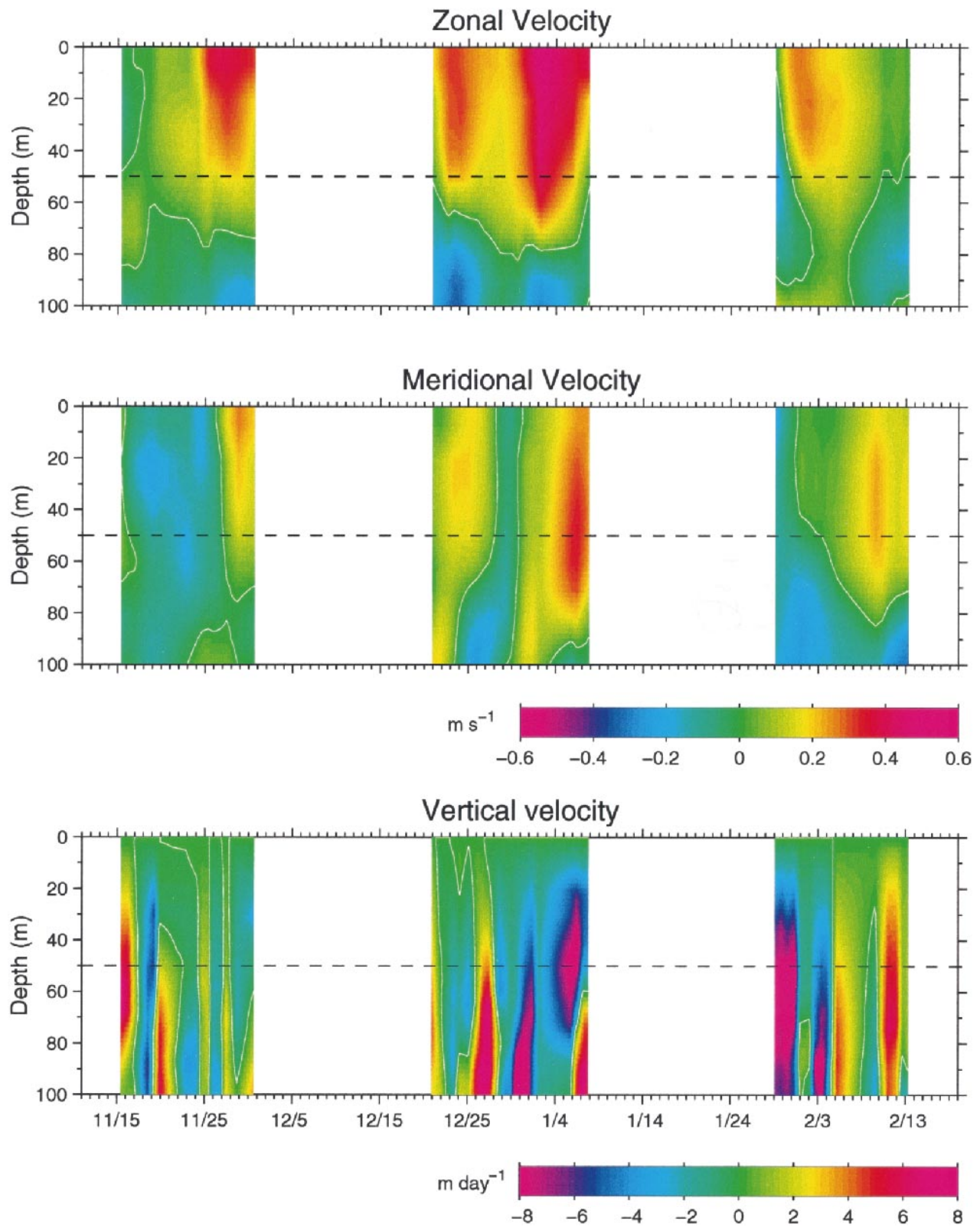


FIG. 4. Zonal (u), meridional (v), and vertical (w) velocities from the repeated survey data linear fits. The 5-m WHOI mooring current meter data are used to interpolate u and v from 20 m to the sea surface. Positive velocities are eastward, northward, and upward. The unit for horizontal velocity is m s^{-1} , and for vertical velocity is m day^{-1} .

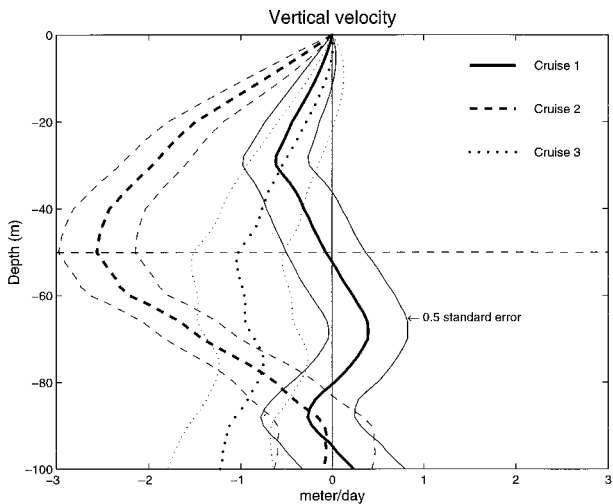


FIG. 5. Cruise-averaged vertical velocity (m day^{-1}) profiles computed as described in the text. The shading indicates half of the standard error at each depth.

line. The isohaline depths undulate consistently with the isothermal depths, indicating dominantly adiabatic displacement in the upper pycnocline. Generally, the thermocline deepens due to WWB-caused convergence and becomes shallower when the westerly relaxes and during the January easterly wind period. The 28°C isotherm reaches its shallowest depth during the easterly recovery between the end of cruise 2 and the beginning of cruise 3 (Eldin et al. 1994). Then, the thermocline deepens quickly at the start of cruise 3 as the next WWB begins (Huyer et al. 1997).

The 0–50-m mean temperature increases by 0.34°C during cruise 1 (Fig. 6), and the 0–50-m layer is stratified by the end of the cruise. The 0–50-m mean temperature decreases sharply by 0.67°C during cruise 2. The temperature also decreases slightly during cruise 3.

The IOP mean horizontal gradients of temperature and salinity in the pycnocline above 100 m are insignificant to the *Wecoma* survey region (Huyer et al. 1997). The horizontal temperature gradient in the 0–50-m layer is typically of the order of $0.1^{\circ}\text{C} (100 \text{ km})^{-1}$. Huyer et al. (1997) found that the standard deviations of the 20-m temperature along both the north-south and west-east *Wecoma* sections are of similar magnitude. This is also consistent with the magnitude derived from the Reynolds and Smith (1994) SST data on larger spatial scales (Ralph et al. 1997). The zonal and meridional gradients vary on a timescale of less than a week, which may not be well resolved in the weekly SST data (Reynolds and Smith 1994). The meridional gradient is negative (cooler to the north) during most of cruise 1 and positive during cruise 2. The magnitude of the horizontal temperature gradient in the upper 50 m decreases with time and there are no significant horizontal gradients during cruise 3, indicating that the temperature field becomes horizontally homogeneous

with time (Fig. 6). The largest upper ocean meridional temperature gradient occurs near the end of cruise 2, with a subsurface peak value of $0.4^{\circ}\text{C} (100 \text{ km})^{-1}$. This is not observed from the weekly SST data (Ralph et al. 1997). While the upper ocean zonal temperature gradient may be due to surface forcing differences over a larger horizontal scale (Ralph et al. 1997), the meridional temperature gradient seems to be more influenced by thermocline processes. The large magnitude of horizontal gradients below 50 m are due to the presence of internal waves that advect the thermocline vertically and that have horizontal scales comparable to the survey domain.

During cruise 1, the mean surface layer salinity decreases (Fig. 7), though there is little rainfall (Table 2). The rain rate is highest during cruise 2 (Table 2), while the mean surface layer salinity increases by nearly 0.1 psu (Fig. 7). This indicates that the salinity changes on the ISO timescale are not controlled directly by the local surface forcing, which is also found in the moored salinity data (Cronin and McPhaden 1998). There is a persistent negative meridional salinity gradient in the upper 50 m during all three cruises, but with decreasing magnitude over time. The zonal salinity gradient changes sign and then becomes weaker with time. Thus, the salinity field also becomes horizontally homogeneous with time. The largest zonal gradient in the upper 0–50 m occurs at the end of cruise 1, with peak magnitude of $0.5 \text{ psu} (100 \text{ km})^{-1}$ near the surface.

c. Advection and budget calculations

1) HEAT

We focus our analysis on the 0–50-m layer, where the three advection terms are mostly smaller than 3 W m^{-3} (Fig. 8). In contrast to Ralph et al. (1997), prominent negative zonal advection occurs during the 25 November westerly wind period of cruise 1, at the beginning of cruise 2, and from 1 January to the end of cruise 2. Occasionally, there is positive zonal advection near the sea surface, but it is not dominant in the 0–50-m average.

Meridional advection has alternating signs during cruise 1, while it is mostly positive during cruise 2 (Fig. 8). Peak meridional advection cools the 0–50-m layer at a rate of more than 100 W m^{-2} after 4 January. This is not observed in the SST-based heat advection estimates (Ralph et al. 1997), likely due to the fact that both the meridional velocity core and the temperature gradient maximum are subsurface. Richards and Inall (2000) have improved their 0–40-m heat budget closure at 2°S , 156°E during the December 1992 WWB period by using the meridional advection from the *Wecoma* calculation. The zonal and meridional advective terms are much smaller during cruise 3 owing to the relatively weak horizontal temperature gradients.

Significant vertical advection mostly occurs below 50

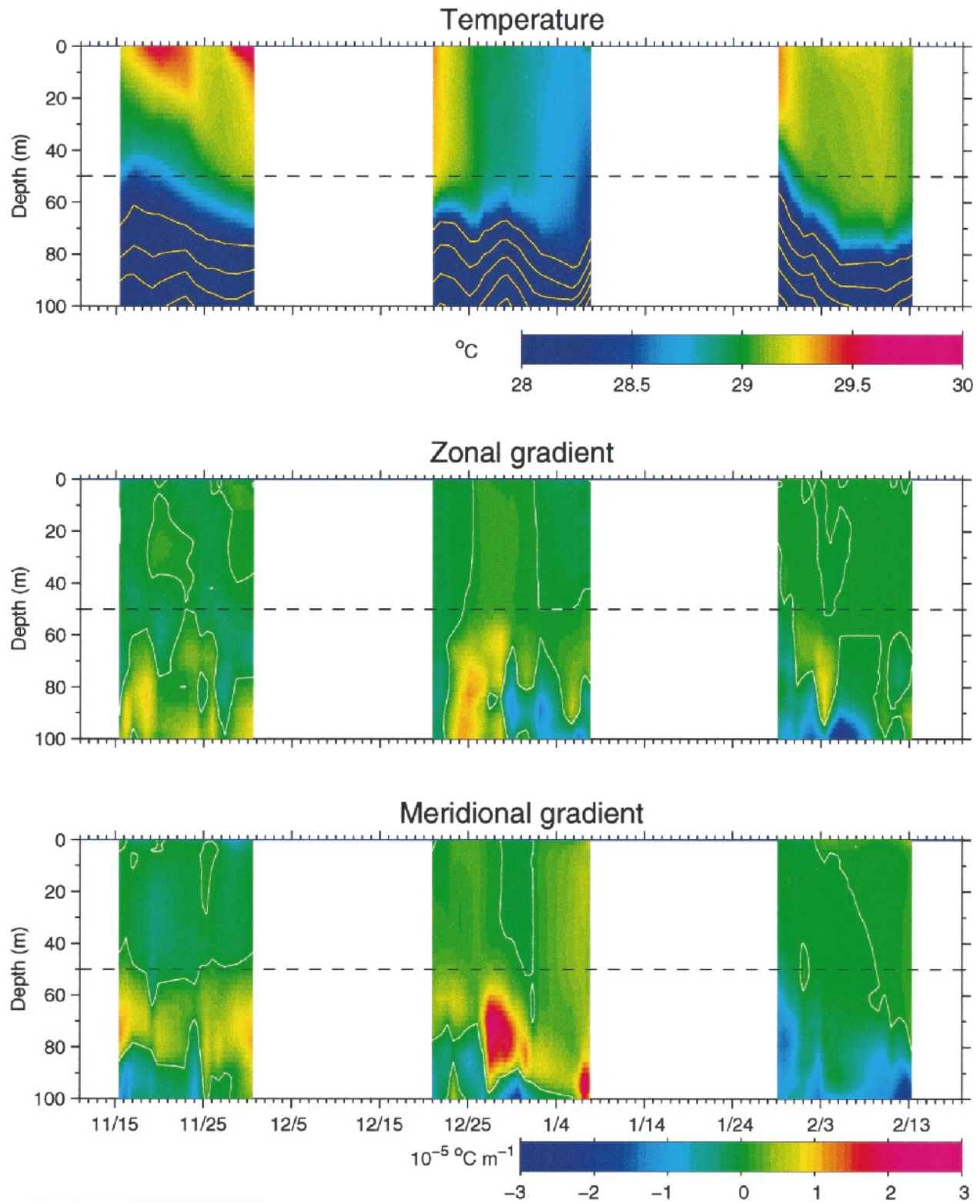


FIG. 6. Temporal evolution of temperature, and zonal and meridional temperature gradients from linear fits of the repeated survey data. The contour interval below 28°C in the temperature plot is 1°C.

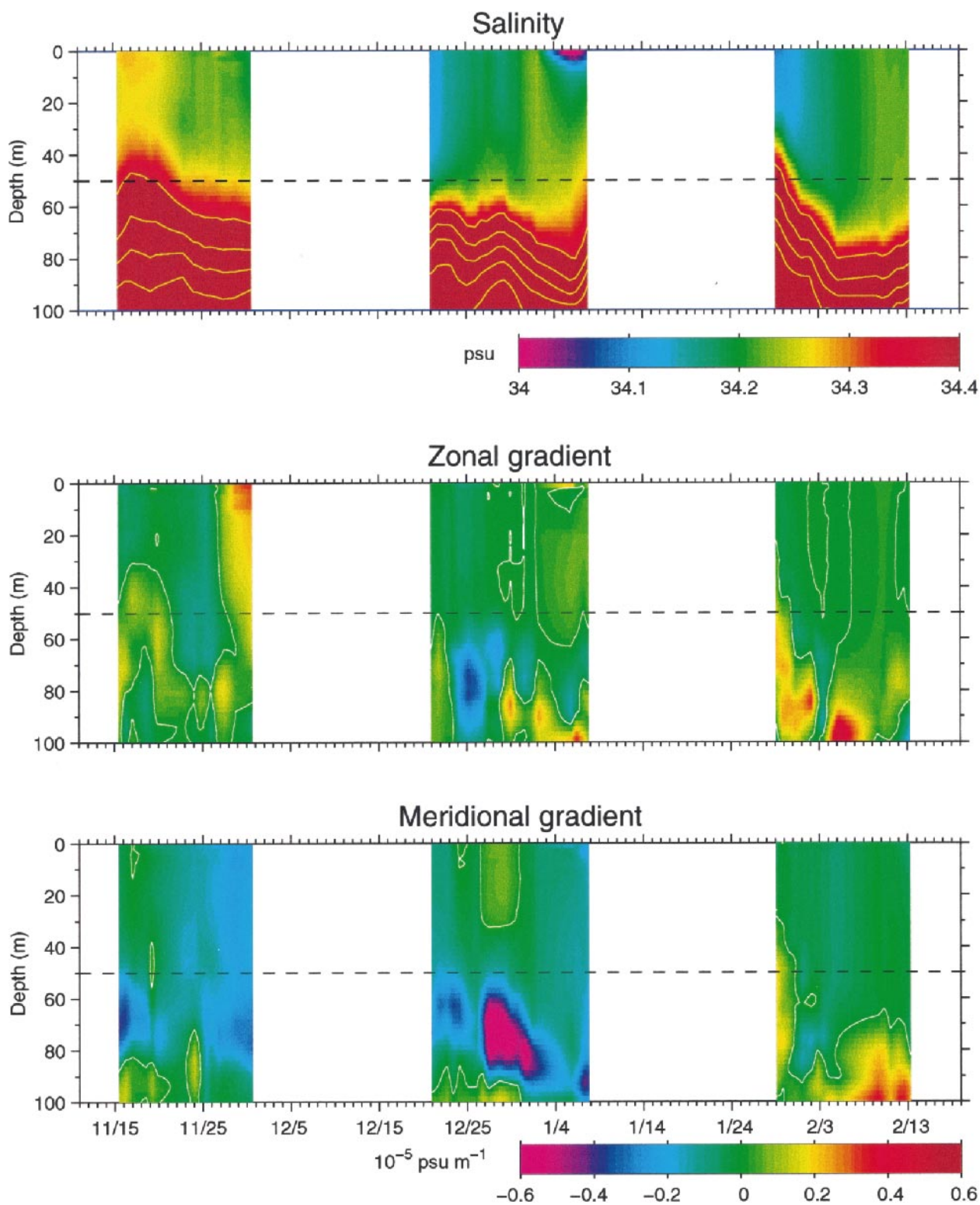


FIG. 7. Temporal evolution of salinity, and zonal and meridional salinity gradients from linear fits of the repeated survey data. The contour interval below 34.4 psu in the salinity plot is 0.2 psu.

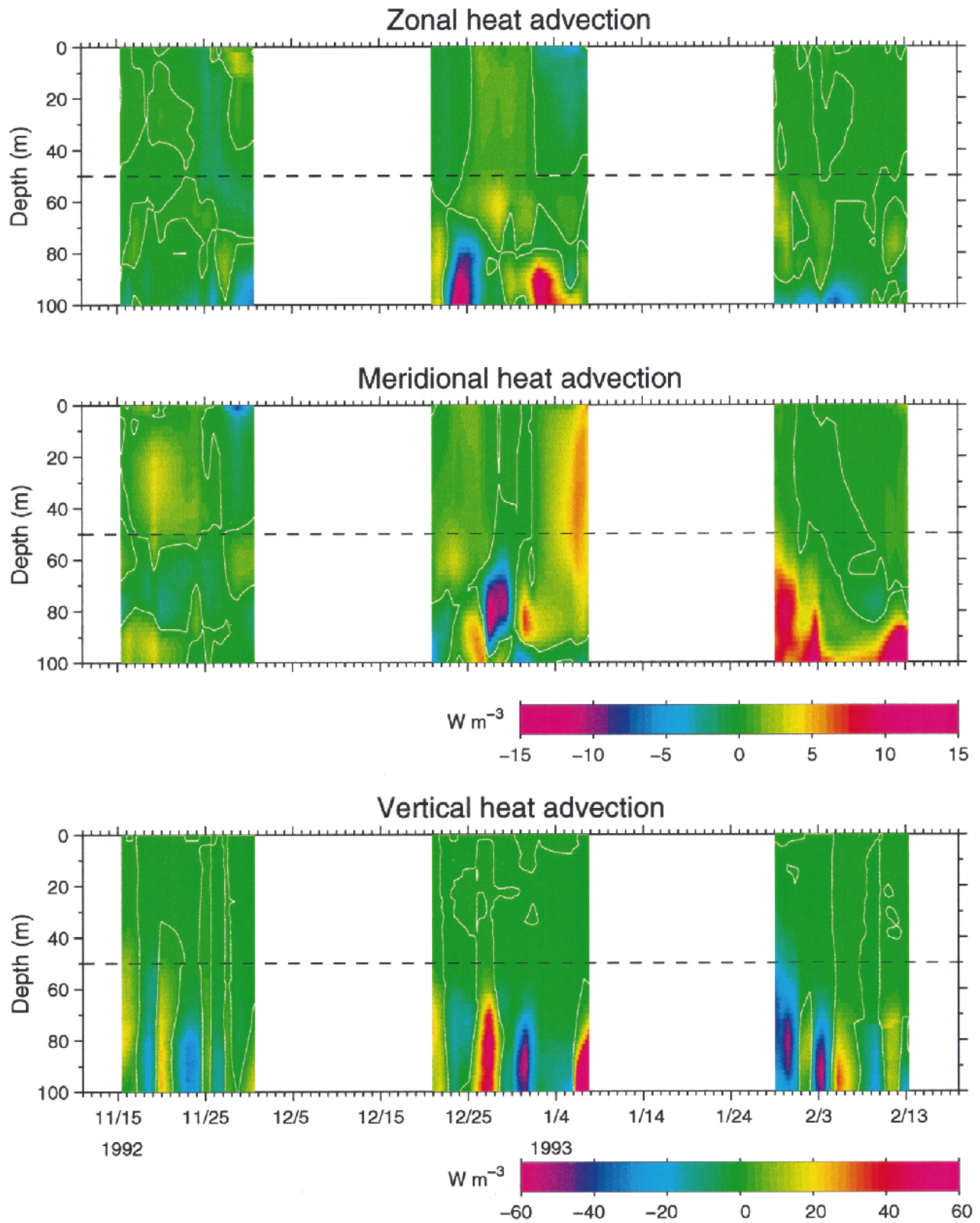


FIG. 8. The zonal, meridional, and vertical components of heat advection from the repeated survey data analysis. Note different scales for horizontal and vertical advective fluxes. The units are $W\ m^{-3}$.

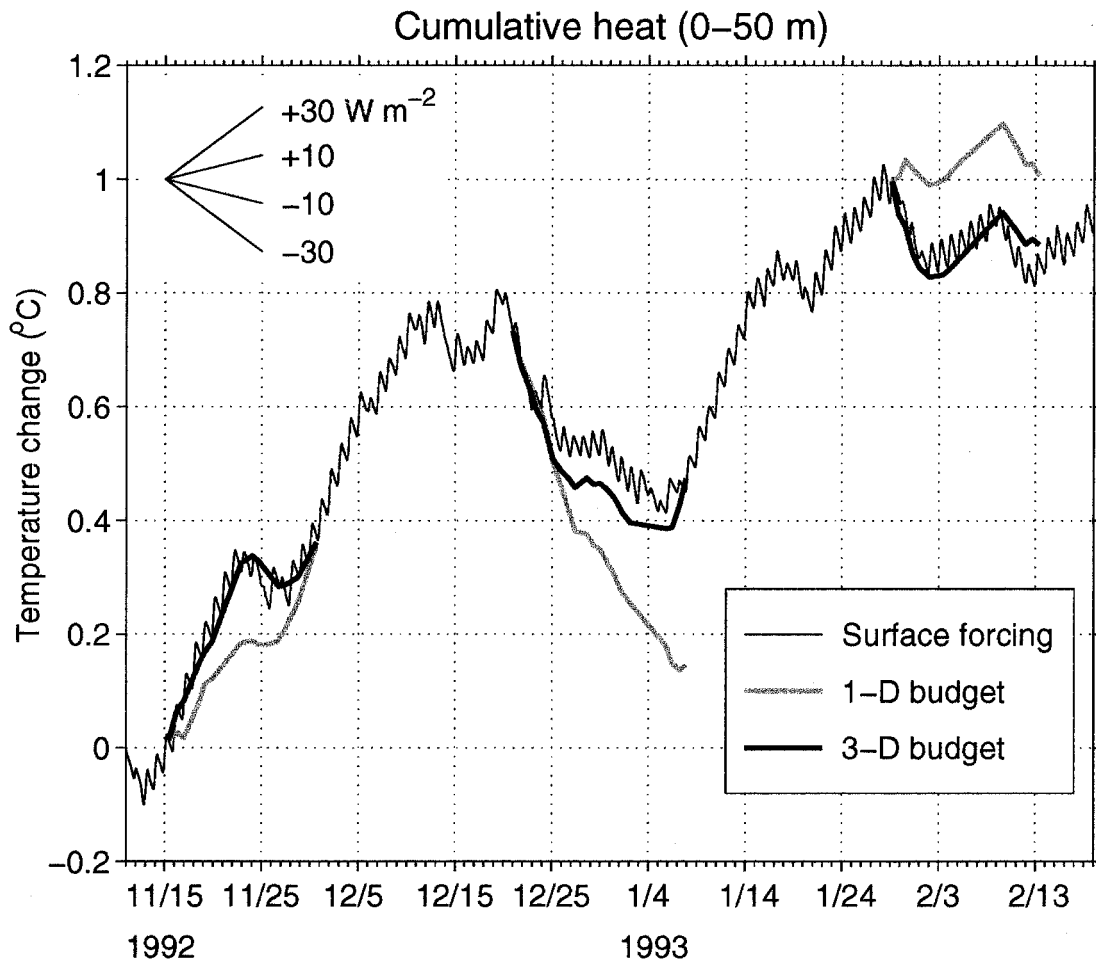


FIG. 9. Cumulative upper-ocean heat budget. The light line is the equivalent temperature change if the surface heat flux forcing (from WHOI mooring data) is applied to the 0–50-m layer; the gray lines are the surface forcing estimated as a residual from the 1D budget; and the heavy lines are the surface forcing estimated from the 3D budget. Note that the gray and heavy lines are shifted to the surface forcing line at the beginning of each cruise. The slopes for equivalent heating are given for reference.

m (Fig. 8). During cruise 3, the largest 0–50-m integrated advective term is vertical advection, having a warming effect of 29 W m^{-2} (Table 2). Note that Richards and Inall (2000) find little contribution from the vertical advection in their 0–40-m heat budget analysis during cruise 3 because they consider a shallower layer and the magnitude of vertical advection increases with depth.

The three heat advection terms integrated over 0–50 m almost cancel out during cruise 1 (Table 1). But without advection, the cumulative heating estimated from the 1D budget deviates from the surface forcing during 23–26 November (Fig. 9). The vertical turbulent heat flux at 50 m is negligible during this cruise (Table 1) because the wind is light and the mixed-layer depth is shallow (Wijesekera and Gregg 1996). Meridional advection dominates over zonal and vertical advection during cruise 2 and the total advection cools the 0–50-m layer at a rate of 43 W m^{-2} (Table 1). When advective

terms are not considered, the estimated cumulative heating in terms of the 0–50-m temperature change is 0.3°C lower than the observed surface forcing (Fig. 9). The 3D budget estimate compares much better with the observations. The net advective heat flux is 18 W m^{-2} during cruise 3, which is also important for closing the heat budget (Fig. 9). Overall, the upper-ocean heat budget is closed within 10 W m^{-2} as cruise means for all three cruises when considering the 3D advective processes (Table 1).

We now separate the mean advection (e.g., $\rho C_p \langle u \rangle \langle \partial T / \partial x \rangle$, where $\langle u \rangle$ and $\langle \partial T / \partial x \rangle$ are cruise averages) and eddy advection [e.g., $\rho C_p \langle u' (\partial T / \partial x)' \rangle$, where the u' and $(\partial T / \partial x)'$ are deviations from the cruise averages] for each cruise (Table 3). The eddy advection here refers to heat advection due to subcruise timescale activity. Because the inertial motion dominates subcruise timescale velocity variability (Fig. 1), the eddy term is presumably dominated by inertial motion con-

TABLE 3. Mean flow and eddy heat advection components during the three cruises.

Component	Cruise 1		Cruise 2		Cruise 3	
	Mean	Eddy	Mean	Eddy	Mean	Eddy
Zonal	-15	6	-7	-6	4	-1
Meridional	14	4	35	30	+1	7
Vertical	-8	0	-6	-3	-6	-23
Total advection	-9	10	22	21	-1	-17

Units: $W m^{-2}$.

tributions. The mean advection represents heat advection due to the ISO and longer timescale variability. A statistically significant estimation of mean/eddy advection would thus require longer observations. During the suppressed phase of the ISO (cruise 1), the mean advection dominates over the eddy advection in all three individual advection terms; however, the total mean advection and eddy advection are of the same magnitudes and have opposite signs. During the active phase of the ISO (cruise 2), the mean and eddy advection have similar magnitudes and the same sign for all three terms, as do their total averages. Meridional advection dominates in both the mean and eddy advection. During cruise 3, the large vertical advection is dominated by the eddy term. Overall, the heat advection due to inertial motions is comparable with or larger than the contributions from the ISO and longer timescale variability.

One difference between the previous estimates of horizontal advection based on SST by Ralph et al. (1997) and the present study is that their calculation was centered on the equator while the center of the survey region analyzed here is near the southern edge of the equatorially trapped eastward jet, and the dynamics are different. From a general circulation model simulation of the upper ocean forced by an idealized WWB centered at the equator, the rectified eastward jet is confined within $2^{\circ}S-2^{\circ}N$ (Kessler and Kleeman 2000). Thus, the heat budget at the center of the IFA ($156.1^{\circ}E, 1.8^{\circ}S$) is less influenced by the zonal flow, while more influenced by the meridional circulation. The other difference is that the multiphase WWB-induced strong inertial motions, which contribute significantly to the heat budget, but these were not resolved in the weekly SST advection calculation.

2) SALT

During cruise 1, zonal advection in the 0–50-m layer tends to bring in saltier water before 26 November and fresher water thereafter (Fig. 10). The cruise average zonal advection is equivalent to a freshwater gain of $7.2 mm day^{-1}$ (Table 2). During cruise 2, zonal advection brings in saltier water before 1 January and reverses sign thereafter.

Due to the alternating meridional current in the surface layer during cruise 1, meridional salinity advection

also alternates sign with time, and tends to compensate for the zonal advection (Fig. 10). During cruise 2, meridional advection is dominated by the two episodes of northward inertial currents in the surface layer, which consistently bring saltier water from the south. Meridional advection is equivalent to a cumulative freshwater loss of $14.8 mm day^{-1}$ (Table 2).

Large vertical salt advection occurs mostly below 30 m. Vertical salt advection is important near the end of cruise 2, and is also large and positive during cruise 3, caused by the downwelling trend during the two cruises.

The net freshwater flux estimated from the 1D budget significantly departs from the surface forcing by more than 100 mm during cruise 1 (Fig. 11). The 3D freshwater budget estimate compares much better with the observed surface forcing. The cumulative effect of advection is to increase the salinity in the upper 50-m layer during cruise 2; the advective effect is equivalent to a mean evaporation rate of $11.5 mm day^{-1}$, or a total freshwater loss of 200 mm (Fig. 11). The freshwater flux estimate during cruise 2 is considerably improved by including the advection terms (Table 2). The net advection of salt is equivalent to nearly 80 mm of rain during cruise 3 and is an important correction to the 1D budget (Fig. 11). Using the estimated evaporation rates from the WHOI mooring and the *Wecoma* data, the estimated average rain rates for each of the three cruises are given in Table 2. These numbers are within approximately 20% of the rain-rate measurements on the *Wecoma*, and fall between the syphon gauge and the ORG numbers, which are believed to respectively underestimate and overestimate the actual rain rate (Bradley and Weller 1997).

The mean and eddy advection components tend to have comparable magnitude in each individual salt advection term for all three cruises (Table 4). In the total advection, the mean term and eddy term tend to compensate with each other. The mean terms are larger during cruises 1 and 2, while the eddy term is larger during cruise 3 due to the strong vertical advection fluctuations.

3) ERROR ESTIMATES

Bootstrap analysis (Efron and Tibshirani 1986) is used to estimate errors in the advective terms (FHL98). Assuming that the errors in the three advective terms are independent, with a decoupling timescale based on autocorrelation calculation, and assuming one degree of freedom in the vertical integration, the standard errors during the three cruises are 12, 11, and $5 W m^{-2}$ for the combined 3D heat advection, and 4, 4, $1.5 mm day^{-1}$ for the combined 3D freshwater advection. The imbalances in the budget calculations are generally within the standard error ranges. Other sources of error such as those in the air–sea fluxes and turbulent fluxes can also contribute to budget imbalances.

In Table 1, the net heat flux is low-pass (2-day cutoff) filtered prior to the temporal averaging. This does not

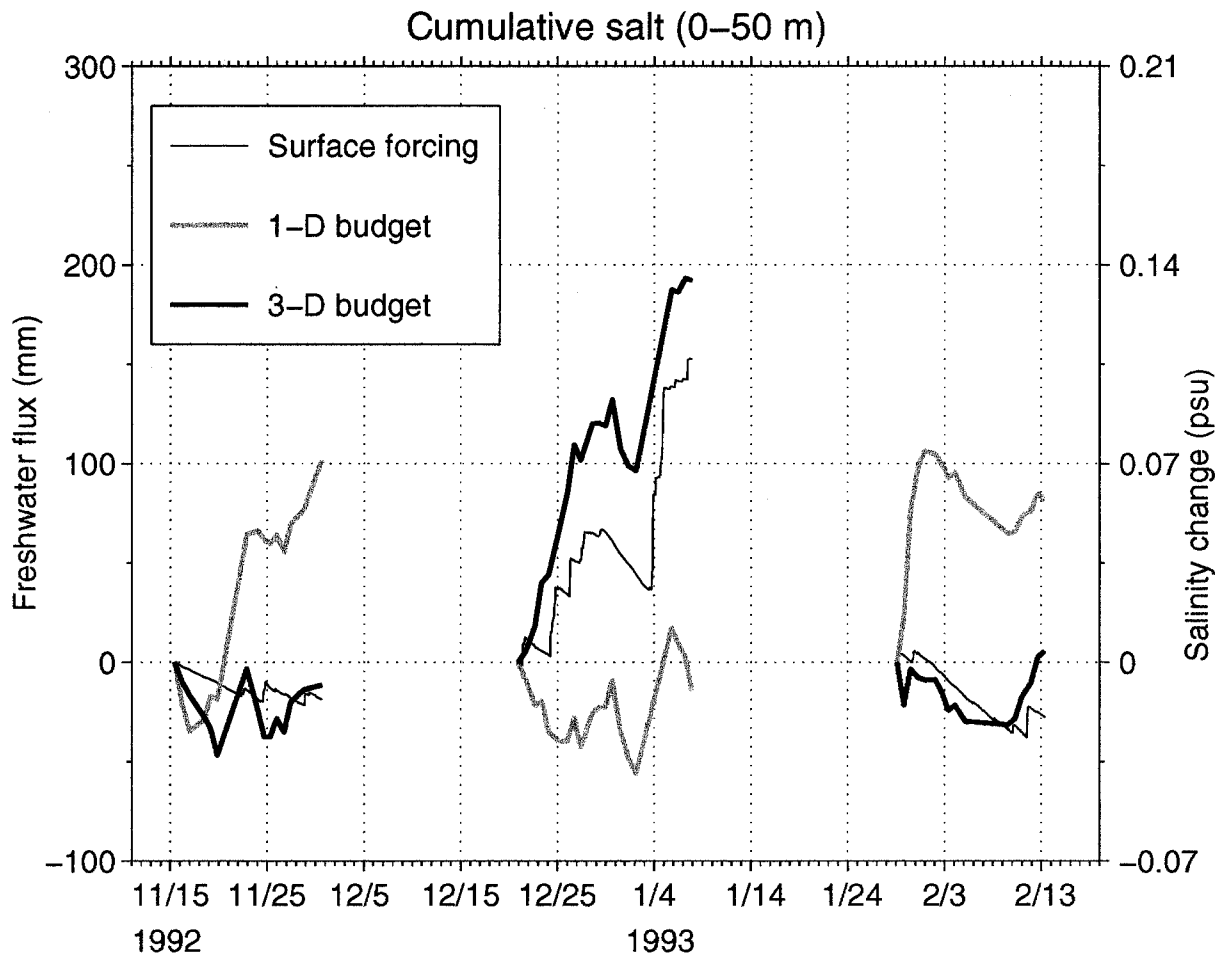


FIG. 11. Cumulative upper-ocean salt budget. The light line is equivalent to freshwater content change if the surface forcing (R/V *Wecoma* syphon data) is applied to the 0–50-m layer; the gray lines are the surface forcing estimated as a residual from the 1D budget; and the heavy lines are the surface forcing estimated from the 3D budget. The right-hand ordinate indicates the equivalent salinity change.

significantly affect the results. No smoothing is applied to the rain-rate and evaporation data. Note that the numbers for cruise 2 in Tables 1 and 2 are slightly different from those in FHL98 due to a change of averaging interval (the time interval for FHL98 analysis is from midnight 19 December 1992 to 7 January 1993 so that there is about a 1-day difference).

4. Discussion and conclusions

On approximately biweekly timescales, with the advective flux and turbulent flux terms included, the heat budget in the surface layer of the warm pool during the COARE IOP balances the air–sea heat flux to within 10 W m^{-2} . The estimated rain rates from the upper ocean salinity budget are within approximately 20% of the rain-rate observations. The advective terms generally cannot be neglected in both the heat and salt balances for all three cruises. Meridional advection tends to cool the surface layer; vertical advection tends to warm the surface layer; and zonal advection alternates, but more

frequently warms the surface layer during the three cruises (Table 1). Meridional advection tends to bring saltier water into the IFA, and vertical advection freshens the upper layer due to the dominance of downwelling during the three cruises (Table 2). Zonal salt advection is only important during cruise 1. The Yoshida jet and inertial motions related to the WWB play major roles in horizontal advection. Both the temperature and salinity fields become horizontally homogeneous with

TABLE 4. Mean flow and eddy salt advection components during the three cruises.

Component	Cruise 1		Cruise 2		Cruise 3	
	Mean	Eddy	Mean	Eddy	Mean	Eddy
Zonal	1.8	5.4	−2.1	0.9	−0.2	−0.9
Meridional	8.2	−8.5	−9.6	−5.2	−3.4	0.5
Vertical	0.8	−0.2	3.1	1.4	1.6	7.4
Total advection	10.8	−3.3	−8.6	−2.9	−2.0	7.0

Units: mm day^{-1} .

time in the surface layer, so that only vertical advection is important during cruise 3. The strong meridional advection found in this study is not noted in equatorial studies using TAO mooring data (Cronin and McPhaden 1998) and the surface drifters (Ralph et al. 1997).

Now we propose a scenario for the WWB-induced meridional advection. During each WWB peak, the meridional current related to the Yoshida jet is equatorward, which causes downwelling at and near the equator and upwelling away from the equator (Gill 1982). The separation between the downwelling and upwelling is at the equatorial Rossby radius, 100–250 km (depending on which vertical mode is involved) off the equator. Far enough off the equator, the pycnocline becomes shallower so that cooler and saltier water is entrained into the surface layer, causing meridional gradients in both temperature and salinity. After the WWB peaks, when the eastward jet turns equatorward due to the Coriolis force, meridional advection brings cooler and saltier water to the equatorial region. In a heat budget calculation right at the equator during the early November 1992 WWB, meridional advection is not evident (Cronin and McPhaden 1997), which may be due to the symmetry of the current or temperature structure at the equator. Note that their mixed-layer temperature at 2°N (2°S) was 0.2°C (0.4°C) cooler than that at the equator shortly after the November 1992 WWB set on. The mooring they used at the equator failed in early December so we cannot compare the advective calculations for the December 1992 WWB. Without considering energetic inertial motions generated by the multiphase WWB, Kessler and Kleeman (2000) are not able to identify the meridional advection contribution to the rectification of the SST.

While the differences between the equator and the *Wecoma* survey site are difficult to quantify with the available data, the case can be made that the *Wecoma* observations are representative of the center of the IFA. The 20–50-m average current velocity from the linear fit of the *Wecoma* data compares well with the daily mean from the WHOI data (Fig. 12), with mean differences of 2.3 and 0.5 cm s⁻¹, and standard deviations of 4.5 and 4.8 cm s⁻¹ for the zonal and meridional components, respectively. We note that the linear fit mean is calculated for the *Wecoma* survey crossover point, and the WHOI mooring is about 10 km to the northwest of that point. The linear fit captures the major velocity signals in the upper ocean on the repeated survey spatial scale, which also rationalizes the advection calculation method. An important discrepancy is near the end of cruise 2 when there is a cyclonic eddy in the surface layer centered south of the butterfly crossover point (Hacker and Lukas 1995; Feng et al. 2000).

The 0–50-m average temperature (linear fit) from the R/V *Wecoma* data agrees very well with the WHOI data during most of the time (Fig. 12). The mean difference between the two is only 0.01°C and the standard deviation is 0.05°C, which is equivalent to a heat flux error

of 3 W m⁻² during 2 weeks. Thus, the heat advection terms calculated from the repeated survey data can be used to explain the misfit between the WHOI data and 1D model (Anderson et al. 1996).

The 0–50-m average salinity from the WHOI mooring varies by about ±0.1 psu during the IOP with a mean value of approximately 34.2 psu (Fig. 12). The linear fit *Wecoma* mean salinity agrees with the WHOI salinity variation on the ISO timescale. There are discrepancies during the second half of cruise 1, at the end of cruise 2, and at the beginning of cruise 3. Also the linear fit mean does not reflect all of the short-term variations seen in the WHOI data. Some rain events, as indicated in the Doppler radar data (Short et al. 1997), were very localized, with spatial scales as small as several kilometers, and short-lived, as the squalls and other small-scale convective activity that they were associated with moved through the IFA. The advective terms calculated from the *Wecoma* data are based on 3-day averages of the spatial survey and are not expected to explain in detail the short-term changes at the WHOI mooring. However, on the ISO timescale our advective flux estimates can be used to explain the lack of agreement between the WHOI mooring data and a 1D model during the three cruises (Anderson et al. 1996).

The linear fit of the repeated survey data is based on the assumption that the dominant spatial scales of the temperature, salinity, and current variations are larger than the survey domain. The near-3-day data fit seems to remove most of the semidiurnal tidal effect (Feng et al. 1998b). However, 2-day oscillations and small-scale eddy activities (Feng et al. 2000) observed during the IOP may alias the linear fit results.

Figure 13 shows the turbulent heat flux at 50 m used in the present study. The turbulent heat flux is downward (negative) most of the time. Upward flux occurs when there is a warmer subsurface layer owing to excessive penetrating solar radiation (Anderson et al. 1996). The positive and negative turbulent heat flux cancels out during cruise 1. The downward flux is larger than the upward flux at the base of the mixed layer (Wijesekera and Gregg 1996). During cruise 2, high downward heat fluxes occur during high-wind and strong-shear episodes. Smyth et al. (1996) estimated a mean heat flux of 18 W m⁻² across near the 28°C isotherm, which is very close to the sum of turbulent flux and penetrating solar radiation across 50 m. Generally, there is a factor of 2 uncertainty when estimating turbulent flux from the microstructure data. During cruise 3, high downward turbulent flux occurs near the end of the cruise. Based on deep AMP measurements, Wijesekera and Gregg (1996) estimated the mean vertical turbulent heat flux below the mixed layer to be 2–10 W m⁻², so that our estimate of the turbulent fluxes during cruise 3 may be an upper bound. However, the budget closure conclusion does not change when we reduce the turbulent fluxes during this cruise (Tables 1 and 2). Note that the measurements of the microstructure data were made only at

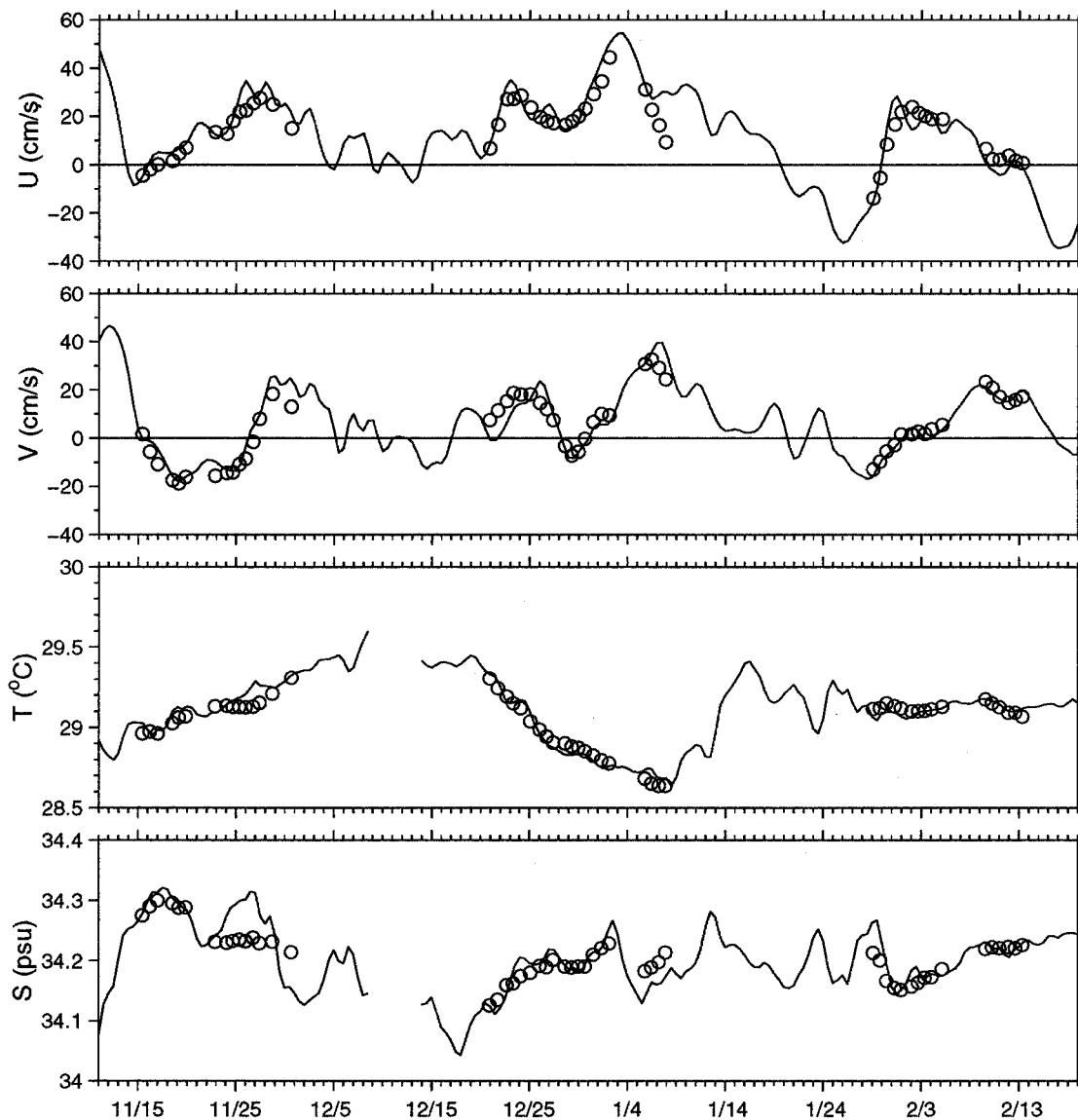


FIG. 12. Comparison of the 20–50-m average current velocity and 0–50-m average temperature and salinity between the WHOI mooring data (daily, solid curve) and the repeated survey data linear fit mean (circles).

one point, while the spatial variations of turbulent mixing may be important in the budget closure.

Still, errors are not a problem in our attempt to close the COARE IOP heat and salt budgets; with the advective terms included, good closure is achieved for the heat and salt budgets for three cruises during different phases of the ISO. Clearly, the availability of good surface fluxes and our ability to resolve horizontal and vertical structure and estimate the vertical advective terms are critical. While variability associated with the ISO in the forcing and in the ocean response is anticipated, the strength of the near-inertial oscillations as well as their dominance in the eddy advective fluxes is a surprise. Our work indicates that the observational campaigns in the upper ocean in the warm pool can, as

in the atmospheric heat and moisture budgets of Lin and Johnson (1996) and Johnson and Ciesielksi (2000), provide independent estimates of the air–sea fluxes of heat and moisture. The agreement achieved in COARE among the oceanic, atmospheric, and direct determinations of the net heat and freshwater fluxes support our belief that the *Wecoma* repeat surveys and associated oceanic measurements are successful in identifying and quantifying the processes most important to the determination of SST in the warm pool.

Acknowledgments. The authors thank Clayton Paulson for providing the *Wecoma* meteorology data; Bill Smyth and Hemantha Wijesekera for providing the *Moana Wave* microstructure data; Eric Firing for pro-

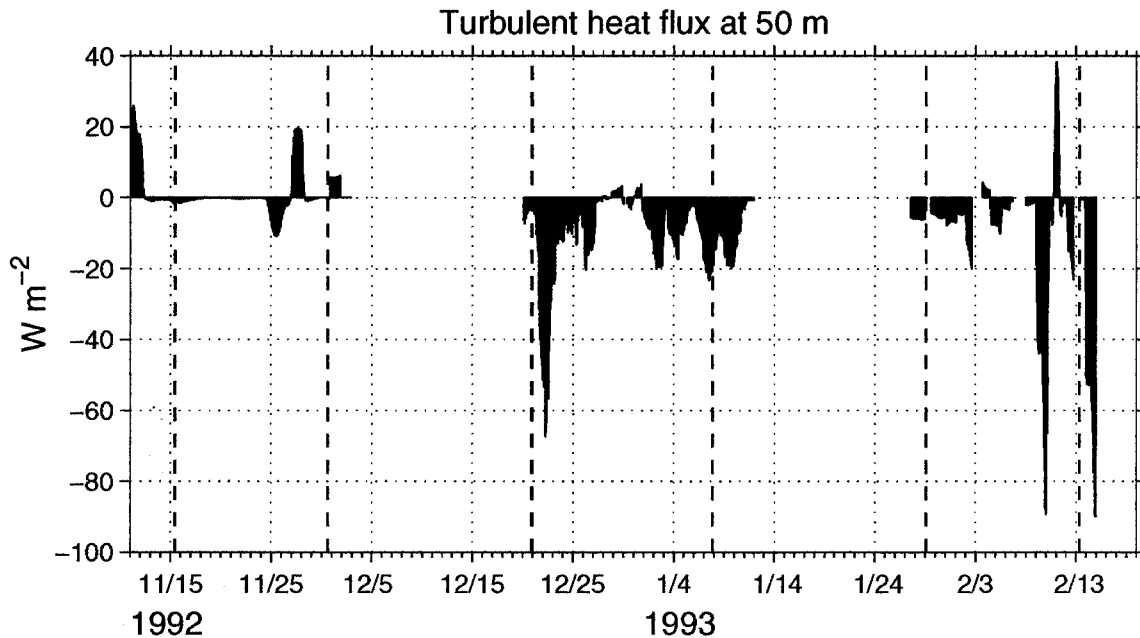


FIG. 13. Vertical turbulent heat flux at 50 m. The vertical dashed lines mark time intervals for budget calculations during the three cruises. Negative values indicate downward heat flux. The units are W m^{-2} .

viding the *Wecoma* ADCP data; all are thanked for their helpful discussions. The authors also thank the reviewers for their valuable comments. Sharon DeCarlo provided excellent computing support during the work. The WHOI buoy was deployed by the WHOI Upper Ocean Processes Group. MF, RL, and PH were supported by the National Science Foundation (NSF) through Grants OCE-9113948 and OCE-9525986 as part of the TOGA COARE program. RAW was supported by NSF Grants OCE91-10559 and ATM95-25844. SPA was supported by NSF Grant ATM95-25844. MF was partially supported by the International Pacific Research Center at the University of Hawaii.

REFERENCES

- Anderson, S. P., R. A. Weller, and R. Lukas, 1996: Surface buoyancy forcing and the mixed layer of the western Pacific warm pool: Observations and 1D model results. *J. Climate*, **9**, 3056–3085.
- Bradley, F., and R. Weller, Eds., 1997: *Fourth Workshop of the TOGA COARE Air–Sea Interaction (Flux) Working Group*. Woods Hole, MA, Woods Hole Oceanographic Institution, 72 pp.
- Cronin, M. F., and M. J. McPhaden, 1997: The upper ocean heat balance in the western equatorial Pacific warm pool during September–December 1992. *J. Geophys. Res.*, **102**, 8533–8553.
- , and —, 1998: Upper ocean salinity balance in the western equatorial Pacific. *J. Geophys. Res.*, **103**, 27 567–27 588.
- Donguy, J., 1987: Recent advances in the knowledge of the climatic variations in the tropical Pacific Ocean. *Progress in Oceanography*, Vol. 19, Pergamon Press, 49–85.
- Efron, B., and R. J. Tibshirani, 1986: Bootstrap methods for standard errors, confidence intervals and other measures of statistical accuracy. *Statist. Sci.*, **1**, 54–77.
- Eldin, G., T. Delcroix, C. Henin, K. Richards, Y. du Penhoat, J. Picaut, and P. Rual, 1994: Large-scale current and thermohaline structures along 156°E during the COARE Intensive Observation Period. *Geophys. Res. Lett.*, **21**, 2681–2684.
- Eriksen, C. C., R. Weller, and R. Weisberg, 1998: Observations of low latitude near-inertial internal gravity waves forced by westerly wind bursts. *AGU Fall Meeting*, San Francisco, CA, Amer. Geophys. Union, 6–10.
- Fairall, C., E. F. Bradley, D. P. Rogers, J. B. Edson, and G. S. Young, 1996: The TOGA COARE bulk flux algorithm. *J. Geophys. Res.*, **101**, 3747–3764.
- , P. O. G. Persson, E. F. Bradley, R. E. Payne, and S. P. Anderson, 1998: A new look at calibration and use of Eppley Precision Infrared Radiometers. Part 1: Theory and Application. *J. Atmos. Oceanic Technol.*, **15**, 1230–1243.
- Feng, M., P. Hacker, and R. Lukas, 1998a: Upper ocean heat and salt balances in response to a westerly wind burst in the western equatorial Pacific during TOGA COARE. *J. Geophys. Res.*, **103**, 10 289–10 311.
- , M. Merrifield, R. Pinkel, P. Hacker, A. Plueddemann, E. Firing, R. Lukas, and C. Eriksen, 1998b: Semidiurnal tides observed in the western equatorial Pacific during TOGA COARE. *J. Geophys. Res.*, **103**, 10 253–10 272.
- , R. Lukas, and P. Hacker, 2000: Spinup of a sub-mesoscale eddy in the TOGA COARE Intensive Flux Array during the spindown of an intense eastward jet. *J. Phys. Oceanogr.*, in press.
- Gill, A. E., 1982: *Atmosphere–Ocean Dynamics*. Academic Press, 662 pp.
- Godfrey, J. S., and E. Lindstrom, 1989: The heat budget of the equatorial western Pacific surface mixed layer. *J. Geophys. Res.*, **94**, 8007–8017.
- , R. A. Houze Jr., R. H. Johnson, R. Lukas, J.-L. Redelsperger, A. Sumi, and R. Weller, 1998: Coupled Ocean–Atmosphere Response Experiment (COARE): An interim report. *J. Geophys. Res.*, **103**, 14 395–14 450.
- Gregg, M. C., D. P. Winkel, and T. B. Sanford, 1994: Internal waves, turbulence, and double diffusion at low latitudes (abstract). *Eos Amer. Geophys. Union*, **75** (Suppl.), 186.
- Hacker, P. W., and R. Lukas, 1995: Spinup of a submesoscale eddy in the TOGA COARE Intensive Flux Array during the spindown of an intense eastward jet. *Abstract, IAPSO XXI General As-*

- sembly, Honolulu, HI, International Association for the Physical Sciences of the Oceans, 444–445.
- Huyer, A., P. M. Kosro, R. Lukas, and P. Hacker, 1997: Upper-ocean thermohaline fields near 2°S, 156°E during TOGA-COARE, November 1992 to February 1993. *J. Geophys. Res.*, **102**, 12 749–12 784.
- Johnson, R., and P. Ciesielski, 2000: Rainfall and radiative heating rates from TOGA COARE atmospheric budgets. *J. Atmos. Sci.*, **57**, 1497–1514.
- Kessler, W., and R. Kleeman, 2000: Rectification of the Madden-Julian oscillation into the ENSO cycle. *J. Climate*, in press.
- Lau, K.-M., and C.-H. Sui, 1997: Mechanisms of short-term sea surface temperature regulation: Observation during TOGA COARE. *J. Climate*, **10**, 465–472.
- Lin, X., and R. Johnson, 1996: Heating, moistening and rainfall over the western Pacific warm pool during TOGA COARE. *J. Atmos. Sci.*, **53**, 3367–3383.
- Lukas, R., and E. Lindstrom, 1991: The mixed layer of the western equatorial Pacific ocean. *J. Geophys. Res.*, **96** (Suppl.), 3343–3358.
- , P. Webster, M. Ji, and A. Leetmaa, 1995: The large-scale context for TOGA Coupled Ocean–Atmosphere Research Experiment. *Meteor. Atmos. Phys.*, **56**, 3–15.
- Moum, J. N., 1990: The quest for K_p . *J. Phys. Oceanogr.*, **20**, 1980–1984.
- Plueddemann, A. J., R. P. Trask, W. M. Ostrom, R. A. Weller, B. S. Way, S. P. Anderson, N. Bogue, J. Shillingford, and S. Hill, 1993: TOGA COARE mooring deployment, check-out, and recovery cruises. Woods Hole Oceanographic Institution Tech. Rep. WHOI-93-30, 54 pp. [Available from Woods Hole Oceanographic Institution, Woods Hole, MA 02543.]
- Ralph, E. A., K. Bi, P. P. Niiler, and Y. du Penhoat, 1997: A Lagrangian description of the western equatorial Pacific response to the wind burst of December 1992: Heat advection in the warm pool. *J. Climate*, **10**, 1706–1721.
- Reynolds, R. W., and T. M. Smith, 1994: Improved global sea surface temperature analyses using optimum interpolation. *J. Climate*, **7**, 929–948.
- Richards, K., and M. Inall, 2000: The upper ocean heat content of the western equatorial Pacific: Processes controlling its change during TOGA COARE. *J. Geophys. Res.*, in press.
- Richardson, R., I. Ginis, and L. Rothstein, 1999: A numerical investigation of the local ocean response to westerly wind burst forcing in the western equatorial Pacific. *J. Phys. Oceanogr.*, **29**, 1334–1352.
- Short, D. A., P. A. Kucera, B. S. Ferrier, J. C. Gerlach, S. A. Rutledge, and O. W. Thiele, 1997: Shipboard radar rainfall patterns within the TOGA/COARE IFA. *Bull. Amer. Meteor. Soc.*, **78**, 2817–2836.
- Siegel, D. A., J. C. Ohlmann, L. Washburn, R. R. Bidigare, C. T. Nosse, E. Fields, and Y. Zhou, 1995: Solar radiation, phytoplankton pigments and the radiant heating of the equatorial Pacific warm pool. *J. Geophys. Res.*, **100**, 4885–4891.
- Skyllingstad, E., W. Smyth, J. Moun, and H. Wijesekera, 1999: Upper-ocean turbulence during a westerly wind burst: A comparison of large-eddy simulation results and microstructure measurements. *J. Phys. Oceanogr.*, **29**, 5–28.
- Smyth, W. D., D. Hebert, and J. N. Moum, 1996: Local ocean response to a multiphase westerly windburst. Part 1: Dynamic response. *J. Geophys. Res.*, **101**, 22 495–22 512.
- Sprintall, J., and M. Tomczak, 1993: Evidence of the barrier layer in the surface layer of the Tropics. *J. Geophys. Res.*, **97**, 7305–7316.
- Webster, P. J., and R. Lukas, 1992: TOGA COARE: The coupled ocean–atmosphere response experiment. *Bull. Amer. Meteor. Soc.*, **73**, 1377–1415.
- Weller, R. A., and S. P. Anderson, 1996: Surface meteorology and air–sea fluxes in the western equatorial Pacific warm pool during the TOGA Coupled Ocean–Atmosphere Response Experiment. *J. Climate*, **9**, 1959–1990.
- Wijesekera, H. W., and M. C. Gregg, 1996: Surface layer response to weak winds, westerly bursts, and rain squalls in the western Pacific warm pool. *J. Geophys. Res.*, **101**, 977–997.
- Zhang, Q., and L. Rothstein, 1998: Modeling the oceanic response to westerly wind bursts in the western equatorial Pacific. *J. Phys. Oceanogr.*, **28**, 2227–2249.